DEFORMATION MEASUREMENT USING INTERFEROMETRIC SAR DATA

M. Crosetto

Institute of Geomatics, Campus de Castelldefels, 08860 Castelldefels (Barcelona), Spain - michele.crosetto@ideg.es

Commission II, WG II/2

KEY WORDS: Remote Sensing, Monitoring, Detection, Modelling, Decision Support.

ABSTRACT:

The paper focuses on the differential interferometric SAR (Synthetic Aperture Radar) technique for the monitoring of terrain surface deformations. The paper begins with a concise description of the properties of the differential interferometric phase, which represents the main observation for the estimation of the deformations. Then the paper discusses of the main features of a new interferometric SAR procedure. In particular, the interferometric SAR processing, the least squares adjustment procedure to estimate the terrain deformations, and the geometric model that is needed to geocode the SAR products are described. The second part of the paper illustrates two applications of the proposed procedure. The first one is a screening analysis, whose main goal is the detection of unknown subsidence phenomena over a large area, based on a limited set of SAR images. The second one is a quantitative analysis of a urban subsidence of small spatial extent, which was based on two independent ascending and descending SAR datasets.

1. INTRODUCTION

This paper addresses the quantitative measurement of terrain deformations using the differential interferometric SAR technique (DInSAR) based on satellite data. For a general review of SAR interferometry, see Rosen et al. (2000). The DInSAR technique has demonstrated its capability to measure deformations in a wide range of applications, which include landslides (Carnec et al., 1996), earthquakes (Massonnet et al., 1993), volcanoes (Amelung et al., 2000), glacier dynamics (Goldstein et al., 1993), and urban subsidences (Amelung et al., 1999). A general discussion of different DInSAR applications can be found in Hanssen (2001). There are different factors that make the DInSAR technique a useful tool for deformation monitoring. Firstly, it is sensitive to small terrain deformations, say up to few millimetres in the best measurement conditions (high image coherence, etc.). Secondly, DInSAR provides a large area coverage, e.g. 100 by 100 km using ERS scenes, with a relatively high spatial sampling density (with a typical 5-look azimuth compression, the ERS images have a 20 by 20 m pixel footprint). The third important characteristic is the availability of large time series of SAR images, that for the ERS satellites cover more than a decade, starting from 1991: with these images it is possible to study the evolution of deformation in the last 12 years. This represents an unmatched capability compared with the traditional geodetic techniques.

An additional characteristic is that DInSAR can (potentially) provide measurements with a quality that is comparable with that of the traditional geodetic techniques. However, this can only be achieved by implementing advanced DInSAR processing and analysis procedures. In fact, besides the deformation component, the DInSAR observations contain different sources of errors: only appropriate modelling and estimation procedures allow the deformations to be estimated with high quality standards. Some of these procedures will be discussed in the following section. In this section we briefly recall the main components of the DInSAR observations.

The interferometric SAR (InSAR) techniques exploit the information contained in the phase of two complex SAR images (hereafter referred to as the master, M, and slave, S, images). In particular, they exploit the phase difference (interferometric phase, $\Delta\Phi_{Int}$) of S and M. Let us consider a point P on the ground, which remains stable in the time interval between the image acquisitions. $\Delta\Phi_{Int}$ is related to the distance difference $SP - MP$, which is the key element for the InSAR DEM generation. When the point moves from P to P^1 between two image acquisitions, besides the topographic phase component Φ_{Topo}, $\Delta\Phi_{Int}$ includes the terrain movement contribution, Φ_{Mov}. In the general case $\Delta\Phi_{Int}$ includes:

$$\Delta\Phi_{Int} = \Phi_S - \Phi_M = \frac{SP - MP}{\frac{\lambda}{4\cdot\pi}} + \frac{SP^1 - SP}{\frac{\lambda}{4\cdot\pi}} + \Phi_{Atm} + \Phi_{Noise} =$$

$$= \Phi_{Topo} + \Phi_{Mov} + \Phi_{Atm} + \Phi_{Noise} ,$$

where Φ_S, Φ_M are the phases of S and M; Φ_{Atm} is the atmospheric contribution; Φ_{Noise} is the phase noise; SP^1 is the slave-to-P^1 distance; and λ is the radar wavelength. If the terrain topography is known (i.e. a DEM of the imaged area is available), Φ_{Topo} can be computed (Φ_{Topo_Sim}) and subtracted from $\Delta\Phi_{Int}$, obtaining the so-called DInSAR phase $\Delta\Phi_{D-Int}$:

$$\Delta\Phi_{D-Int} = \Delta\Phi_{Int} - \Phi_{Topo\_Sim} =$$

$$= \Phi_{Mov} + \Phi_{Atm} + \Phi_{Res\_Topo} + \Phi_{Noise} \qquad (1)$$

where Φ_{Res_Topo} represents the residual component due to DEM errors. In order to derive information on the terrain movement, Φ_{Mov} has to be separated from the other phase components. The best results are achieved when multiple interferograms of the same scene are available.

In the following sections the strategy implemented at the Institute of Geomatics to estimate the terrain deformations from time series of SAR images is described. In the second part of the paper two examples of DInSAR analysis based on stacks ERS SAR images are illustrated. The first one is a screening analysis, which allows unknown subsidence phenomena over large areas to be detected using a limited set of images. The second one is a quantitative analysis of a subsidence of small spatial extent due to mining activity, which is based on ascending and descending datasets.

Figure 1: Amplitude SAR image (left) and coherence image (right) of an interferogram with $\Delta T = 210$ days, where the dark pixels correspond to low coherence areas. The images cover the airport and a small portion of the metropolitan area of Barcelona (Spain).

2. A DInSAR PROCEDURE BASED ON IMAGE STACKS

The key factor to achieve a quantitative DInSAR deformation monitoring is the number of available SAR images over the same study area. The classical DInSAR technique is based on two SAR images, i.e. a single interferogram. With this simple configuration is not possible to separate the deformation contribution from the other phase components. In this work we describe a new DInSAR procedure, which is based on multiple interferograms over the same scene (image stacks). Three main aspects of the procedure are discussed below: the interferometric processing steps to exploit SAR image stacks; the least squares procedure employed to estimate the terrain deformation; and the DInSAR geometric aspects, which affect the computation of Φ_{Topo_Sim} and the geocoding of the DInSAR products.

2.1 Interferometric processing

In order to derive deformation maps from stacks of complex SAR images, the original SAR data have to undergo several processing steps, see e.g. Crosetto et al. (2003). In this section we briefly discuss two important steps: the image co-registration and the phase unwrapping. Another key step, the simulation of Φ_{Topo_Sim}, is concisely discussed in section 2.3.

In order to exploit the phase information of a series of complex SAR images covering the same area, it is necessary to accurately co-register all images over the same master image, arbitrarily chosen as geometric reference. It is worth noting that this operation only concerns the geometric reference: after the co-registration each interferogram can be chosen by taking as master image M any of the co-registered SAR image. Note that other techniques, e.g. (Ferretti et al., 2000; Ferretti et al., 2001), use the same master for all the interferograms. A second key step of the procedure is the phase unwrapping, which is based on an implementation of the Minimum Cost Flow method of Costantini et al. (1999). The most relevant property of this unwrapping is that it works on irregular networks of sparse pixels. The unwrapping is only performed on the pixels whose coherence is above a certain threshold, while it is not computed over low coherence pixels, where it is expected to have high Φ_{Noise} values. With this procedure the long-term deformation monitoring is limited to the areas that remain coherent over long time periods. This typically occurs over urban, suburban and industrial areas. An example is illustrated in Figure 1, where on the amplitude image (left) on may recognize different

man-made structures: urban and industrial areas (bright amplitude values), and the runways of the Barcelona airport (dark). All these structures are characterized by high coherence values (Fig. 1, right), while the rural areas and the water surfaces show low coherence values.

2.2 Least Squares adjustment

Let us assume that from a stack of co-registered SAR images a set of N differential interferograms has been computed. For each pixel that remains coherent over the observation period it is possible to write N equations (1), one for each interferogram. In order to estimate the terrain movement, Φ_{Mov} has to be separated from the other components: $\Phi_{Re\,s\_Topo}, \Phi_{Atm}$ and Φ_{Noise}. Different modelling and estimation procedures can be employed for this purpose. Without going into technical details, we briefly discuss some important issues of our procedure.

The residual component due to DEM errors $\Phi_{Re\,s\_Topo}$ has a known geometric relationship with the DEM error, e_{DEM}:

$$\Phi_{Re\,s\_Topo} = \frac{4 \cdot \pi \cdot B_\perp}{MP \cdot \sin\Theta} \cdot e_{DEM} \qquad (2)$$

where $B_\perp$ is the normal baseline and Θ is the off-nadir angle. For each coherent pixel of the N interferograms we have an unknown parameter e_{DEM}. Since its effect in each interferogram is modulated by $B_\perp$, the wider is the spectrum of $B_\perp$, the better is the configuration to estimate e_{DEM}.

Modelling the terrain deformation represents a quite complex task. In fact, in principle we need a 3D model, with two dimensions in the image space, plus a component to describe the temporal evolution of the deformation. A general discussion of 3D models for DInSAR analysis is beyond the scope of this paper. We just mention that often the temporal evolution of the deformation is modelled with polynomial functions of the time. In our procedure the deformation of each pixel is modelled by a stepwise linear function, which is computed by least squares (LS) adjustment.

Different approaches to estimate the atmospheric component have been proposed, see e.g. Ferretti et al. (2000). In order to separate Φ_{Mov} and Φ_{Atm} the following property is often employed: both components are (usually) spatially correlated,
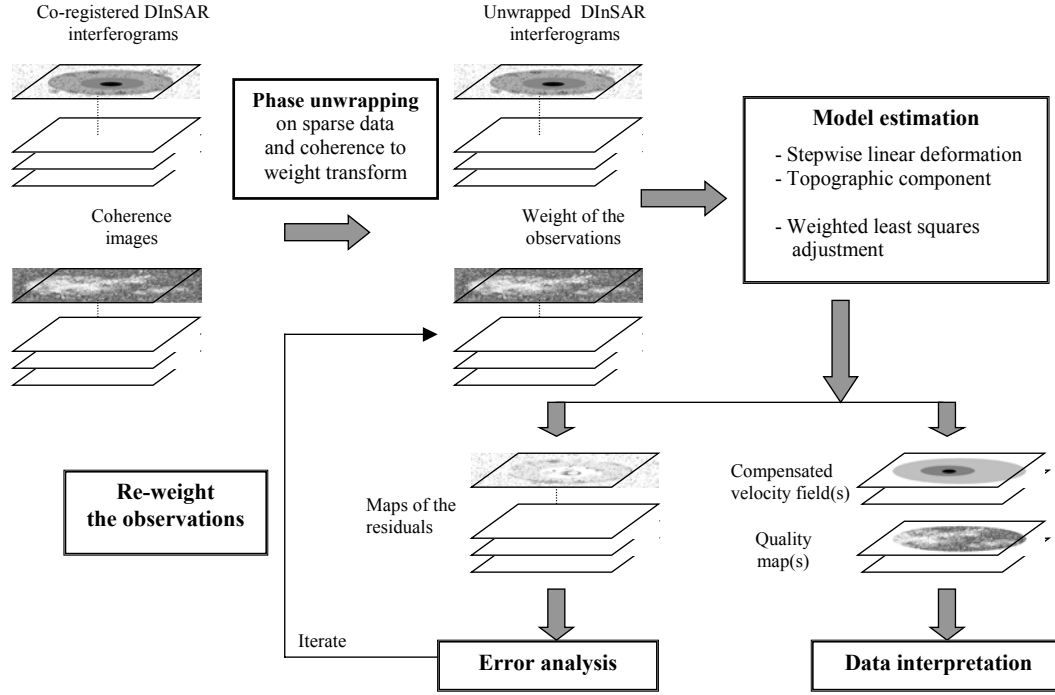
Figure 2: Scheme of the LS adjustment procedure based on multiple interferograms.

Φ_{Mov} is usually temporally correlated, while the atmospheric effects are supposed to be uncorrelated in time. A specific strategy can be implemented dealing with small-scale deformations, when a priori information on the subsidence area is available, see Crosetto et al. (2002).

The main features of the DInSAR estimation procedure employed in this work are briefly summarized below. The implemented model includes for each pixel the DEM error and a stepwise linear function to describe the temporal evolution of the deformation. The unknown parameters are computed by LS adjustment. A scheme of the procedure is shown in Figure 2. The procedure supports the classical data snooping proposed by Baarda (1968), useful to detect the unwrapping-related errors. The outputs of the procedure include the compensated velocity fields, the corresponding quality maps (with the standard deviations of the velocities), and the maps of the residuals. It must be noted that in the so-called screening analysis, which is based on a reduced set of images, usually only one velocity field is estimated: different intervals can be considered in the subsequent in-depth analysis based on larger datasets. The residuals are used to check the errors associated with the unwrapped interferograms (i.e. the input observations), like the unwrapping-related errors, the atmospheric effects, etc. In order to improve the estimates of the compensated velocity fields, the procedure can be run iteratively, by re-weighting the observations or eliminating some of them.

2.3 Geometric aspects

The DInSAR technique requires an accurate geometric model to connect the SAR image space to the object space. This geometric model is required in two key processing stages: the computation of Φ_{Topo_Sim}, based on a DEM of the imaged scene, which involves the object-to-image transformation, and the geocoding of the DInSAR products, which is based on the image-to-object transformation. In our procedure we have implemented a rigorous SAR model that connects the image

coordinates of a given pixel, azimuth and range (az, rg), to the object space coordinates P(X,Y,Z) with three equations:

$$T = T_0 + \Delta T \cdot (az\text{-}1) \tag{3}$$

$$MP = R_0 + \Delta R \cdot (rg\text{-}1) \tag{4}$$

$$\overline{MP} \cdot \overline{V}_M = -\lambda \cdot MP \cdot \frac{f_{D\_M}}{2} \tag{5}$$

where (3) provides the time of acquisition T of a given image point (az, rg); (4) and (5) are the two basic SAR mapping equations, namely the range and Doppler equations. These equations include important parameters like the first line acquisition time T_0, the azimuth pixel size ΔT, the near slant range R_0, the range pixel size ΔR, the master velocity vector V_M, the radar wavelength λ, and the Doppler frequency of the master image f_{D_M}. These parameters are usually known with an inadequate accuracy. Their direct use in the model may result in important distortions in the transformations between the image and object spaces. In order to get an accurate geometric model, the model parameters have to be refined by LS adjustment using ground control points (GCPs). The original implementation of the calibration worked with one image at the time. The procedure is now extended in order to fuse data coming from multiple images, e.g. ascending and descending SAR images. The multiple adjustment allows reducing the number of required GCPs using tie points, in full analogy with the photogrammetric procedures. After the LS calibration, the residuals on the GCPs are typically of the order of one pixel: using a 5-look azimuth compression this corresponds to about 20 m on the ground, see e.g. Crosetto et al. (2003). It is worth mentioning that other SAR calibration strategies can be implemented. One of the most interesting approaches only requires as input a DEM of the scene. The calibration of T_0 and R_0 is achieved by image correlation of the given SAR image and a synthetic amplitude image simulated from the DEM. This approach is implemented in different softwares, e.g. the DIAPASON software developed by the French CNES.
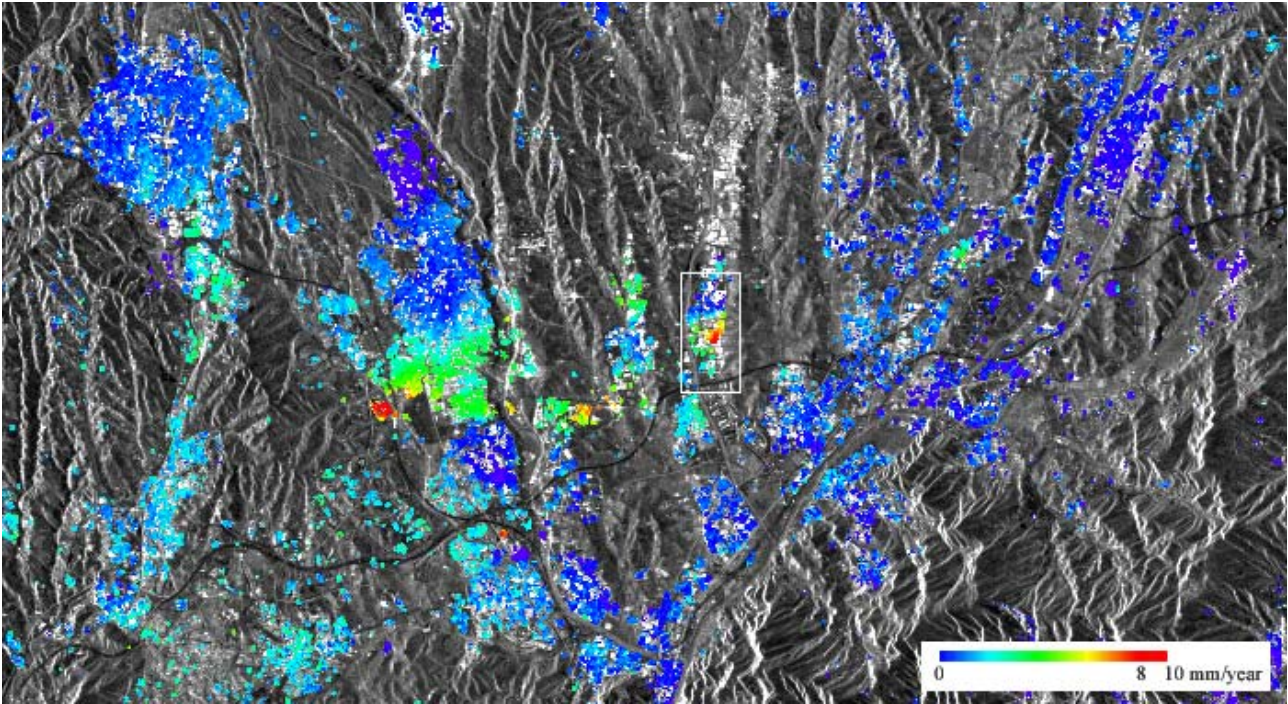
Figure 3: Result of the screening analysis over an area of 28 by 12 km based on 10 ERS interferograms. The deformation velocity field, which was estimated between June 1995 and August 2000, is superposed to a SAR amplitude image of the same area.

3. DISCUSSION OF RESULTS

The above described DInSAR procedure can be employed in different operational contexts. In this paper we describe two applications. The first one is a screening analysis, which allows unknown subsidence phenomena over large areas to be detected using a limited set of SAR images. In this application the major emphasis is on the "early detection" of unknown deformations, rather than on a quantitative estimation of the deformations. For this reason, the analysis can be performed using a limited SAR dataset. This low-cost deformation detection takes full advantage of the wide area coverage of the SAR images, which typically cover 100 by 100 km. The second type of application is a quantitative analysis of an already known deformation area: a urban subsidence of small spatial extent due to mining activity.

The above described screening procedure was used over a test area of about 340 km^2, which is located in Catalonia (Spain), where no a priori information on land deformation was available. The analysis was based on 10 interferograms, which were computed from 13 ERS ascending SAR images. These images cover more than five years, from June 1995 to August 2000. The interferograms have different values of temporal baseline (the time interval between the acquisitions of M and S), which span from 630 days up to 1750 days. The test areas is shown in Figure 3, where the deformation velocity field is superposed to a SAR amplitude image. As it could be expected, most of the considered region shows no deformation. However, there is a relatively big area of about 4 km^2 with is characterized by a deformation rate of about 5 mm/yr, and other deformation areas of small spatial extent, which show deformation rates up to 10 mm/yr. It is worth noting that this only represents a first detection of these subsidences, whose actual importance will be assessed in the future. However, this example shows the potential of DInSAR as an "early detection tool" of deformations.
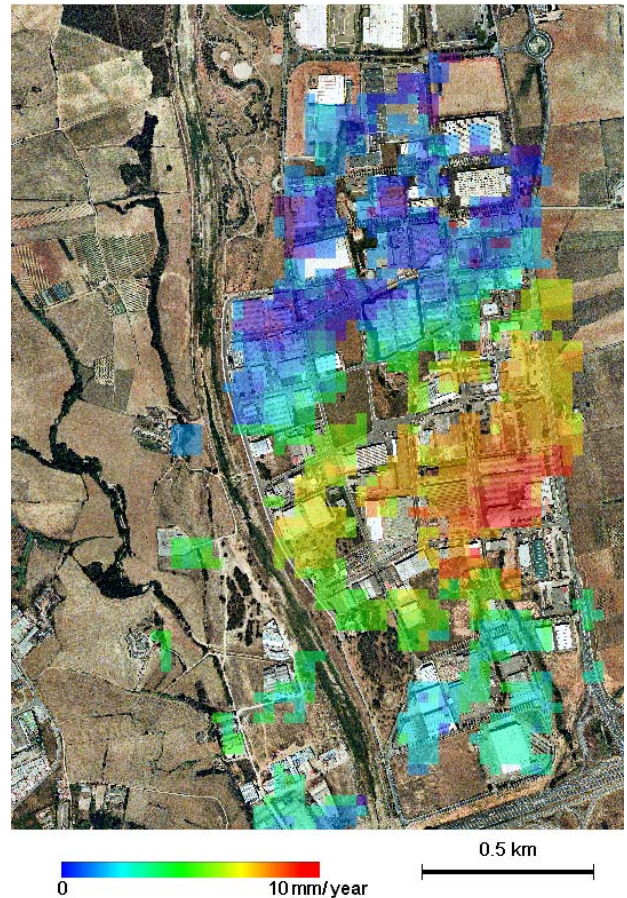

Figure 4: Result of the screening analysis over an industrial area, whose location is shown by a white frame in Figure 3. The deformation velocity field is superposed to a 1:5000 orthoimage of the Cartographic Institute of Catalonia (ICC).
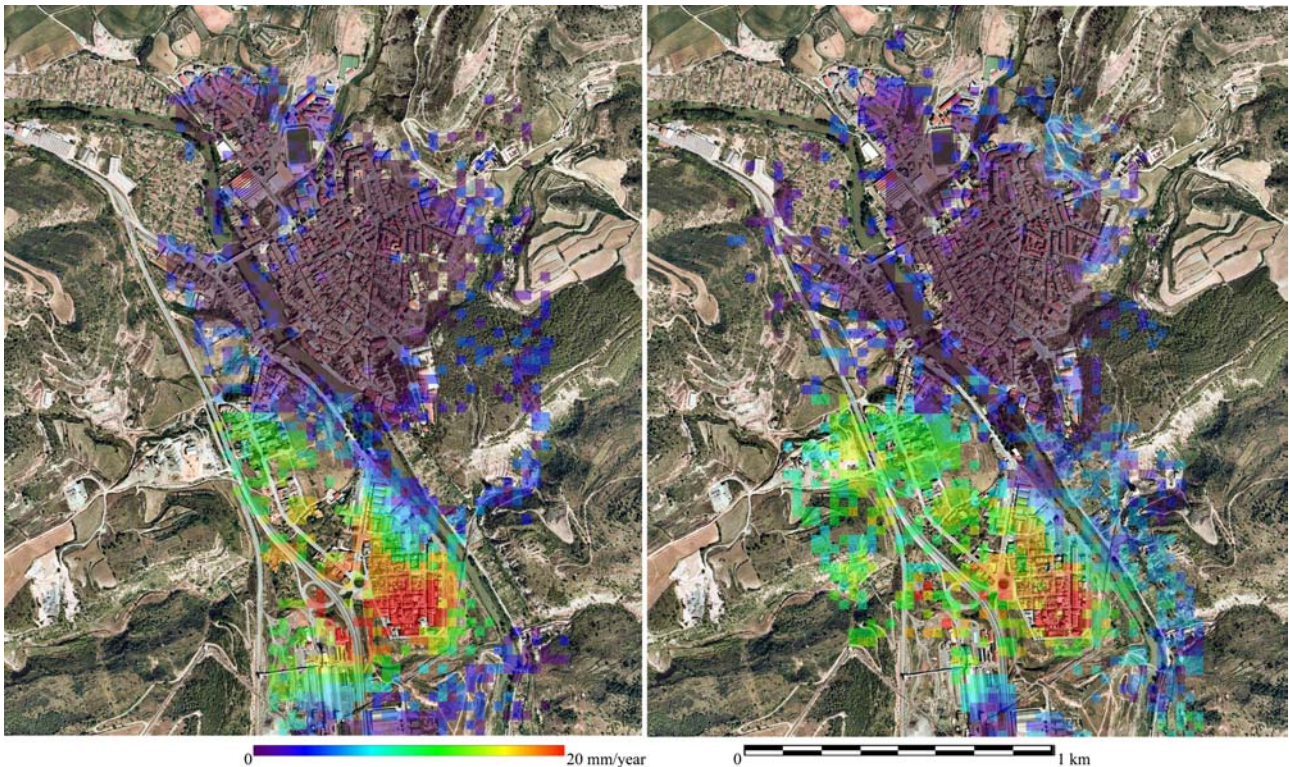
Figure 5. Results of the DInSAR analysis of the subsidence of Sallent (Spain), based on two independent datasets. Left image: geocoded mean velocity fields over about five years, estimated with 13 ascending interferograms. Right image: geocoded mean velocity fields over the same period, which was estimated with 14 descending interferometric pairs. The two fields are superposed to a 1:5000 orthoimage of the Cartographic Institute of Catalonia (ICC).

As already mentioned in the introduction, one of the most important characteristic of DInSAR is its capability to provide a wide area coverage, say 100 by 100 km, associated with a high sampling density (20 by 20 m pixel footprint with a 5-look compression). This property is illustrated in Figures 3 and 4. In Figure 3 one may appreciated the wide area coverage of the screening analysis, which includes several cities and villages over an area of about 340 km^2. Figure 4 shows a zoom of the results of Figure 3 over an industrial area of less than one square kilometre. In this case one may appreciate the high spatial resolution of the velocity field, which allows the analysis of deformation phenomena of small spatial extent to be performed. In this case the pixels have a 40 by 40 m footprint, since a compression of 10 by 2 looks was used. It is important to underline that the results shown in Figure 3 and 4 come from the same input data and the same LS adjustment. The differences are related to the scales of the two images and the way the results are visualized. In fact, in Figure 3 the deformation velocity field is represented in the image space, superposed to an amplitude SAR image, while Figure 4 shows a geocoded deformation velocity field (i.e. a DInSAR product given in the object space) superposed to a orthoimage. This last type of visualization, which needs a image-to-object transformation and hence the calibration of the geometric model, represents the key factor to exploit the DInSAR products.

The second example considered in this work is the quantitative analysis of a known urban subsidence of small spatial extent, located in the village of Sallent (Spain). A portion of the village, which lies on an old pottassic salt mine, is subjected to subsidence, which is mainly caused by

water filtration in the salt layers. This area has been already studied by DInSAR, see Crosetto et al. (2002) and Crosetto et al. (2003). The Sallent subsidence, which affects an area of less than one km^2, was analysed using two ascending and descending SAR datasets, in order to derive two independent estimates of the same deformation field. The two datasets cover the same period, from 1995 to 2000, and include 14 ascending and 13 descending ERS interferograms. The two geocoded mean velocity fields, superposed to an orthoimage at scale 1:5000, are shown in Figure 5. One may notice that the two fields show a quite similar pattern. There are small differences in their area coverage, which are mainly due to the different image acquisition geometries. The quantitative comparison of these results is described in Crosetto et al. (2003b). In general, there is a good agreement between the two estimated velocity fields: despite the small number of interferograms (13 for the descending dataset) the obtained results show a good consistency. A further step in the analysis of this subsidence will be the estimation of its temporal evolution, by fusing the observations coming from the ascending and descending datasets.

4. CONCLUSIONS

The DInSAR technique can provide deformation measurements with a quality that is comparable with that of the traditional geodetic techniques. This capability, which can only be achieved by implementing advanced DInSAR processing and analysis procedures, is associated with three other important features of this remote sensing technique: the wide area coverage, the high spatial resolution, and the availability of large historical SAR datasets that for the ERS

satellites cover the last 12 years. In this paper, the most relevant aspects of a flexible DInSAR procedure for deformation measurement have been discussed. The procedure works with multiple interferograms over the same scene, i.e. with stacks of SAR images. This represents the key factor to achieve quantitative DInSAR deformation monitoring capabilities. Three main aspects of the procedure have been discussed. Firstly, the interferometric procedures to process SAR image stacks, which include a phase unwrapping algorithm that works on irregular networks of sparse pixels. With this algorithm, only the pixels that remain coherent over the observation period (say, few years) are used. This limits the deformation monitoring to the areas that remain coherent over long periods, like the urban, suburban and industrial areas. Secondly, the least squares adjustment employed to estimate the deformations has been illustrated. The estimation strategy has been described, detailing few important aspects of the modelling of the phase components, like the residual topographic component and the atmospheric contribution. Thirdly, the DInSAR geometric aspects have been addressed, emphasizing the importance of the geometric model, which connects the SAR image space to the object space. This model plays a key role in the geocoding of the DInSAR products. A rigorous SAR model has been briefly described. In our procedure an accurate geometric model is achieved by refining the model parameters by LS adjustment using GCPs.

Two applications based on the proposed DInSAR procedure have been described. The first one is a screening analysis, whose main goal is the detection of unknown subsidence phenomena using a limited set of SAR images. The second one is a quantitative analysis of a urban subsidence of small spatial extent. Without any a priori information on the analysed area, which has an extension of 340 km^2, using 10 ascending interferograms, different deformation areas have been detected. This result shows the great potential of the technique to perform a fast and low-cost deformation analysis over large areas. The analysis of the subsidence of small spatial extent has been based on two independent SAR datasets. Despite the relatively reduced number of available observations (13 and 14 interferograms for the ascending and descending dataset, respectively), the two derived velocity fields are very consistent, both in terms of shape and magnitude of the estimated deformations. This confirms the capability of DInSAR to quantitatively assess deformation phenomena, and opens the possibility to exploit this technique in different applications and operational contexts. This is also confirmed by the great number of projects that are based on the DInSAR technique, see e.g. (Strozzi et al., 2001; and Colesanti et al., 2003).

The main limitation of the DInSAR technique is that it only provides information on the urban and industrial areas, which however represent a very important type of land cover, where most of the economical and social activities are concentrated. The capabilities of the procedure described in this paper will be improved in the future. A first step will be the joint estimation of the deformations by fusion of the ascending and descending datasets. A further step will include advanced 3D modelling tools to separate the deformation phase component from the atmospheric contribution.

REFERENCES

Amelung F., Galloway D.L., Bell J.W., Zebker H.A., Laczniak R.J., 1999. Sensing the ups and downs of Las Vegas: InSAR reveals structural control of land subsidence and aquifer-system deformation. *Geology*, Vol. 27, No. 6, pp. 483-486.

Amelung F., Jonson S., Zebker H.A., Segall P., 2000. Widespread uplift and 'trapdoor' faulting on Galápagos volcanoes observed with radar interferometry. *Nature*, Vol. 407, pp. 993-996.

Baarda W., 1968. A testing procedure for use in geodetic networks. Netherlands Geodetic Commission, Publications on Geodesy, Vol. 2, No. 5, Delft (Holland).

Carnec C., Massonnet D., King C., 1996. Two examples of the use of SAR interferometry on displacement fields of small spatial extent. *Geophysical Research Letters*, Vol. 23, No. 24, pp. 3579-3582.

Colesanti C., Ferretti A., Prati C., Rocca F., 2003. Monitoring landslides and tectonic motions with the Permanent Scatterers Technique. *Engineering Geology*, Vol. 68, pp. 3-14.

Costantini M., Farina, A., Zirilli F., 1999. A fast phase unwrapping algorithm for SAR interferometry. *IEEE Transactions on Geoscience and Remote Sensing*, Vol. 37, No. 1, pp. 452-460.

Crosetto M., Tscherning C., Crippa B., Castillo M., 2002. Subsidence monitoring using SAR interferometry: reduction of the atmospheric effects using stochastic filtering. *Geophysical Research Letters*, Vol. 29, No. 9, pp. 26-29.

Crosetto M., Castillo M., Arbiol R., 2003. Urban subsidence monitoring using radar interferometry: Algorithms and validation. *Photogrammetric engineering and remote sensing*, Vol. 69, No. 7, pp. 775–783.

Crosetto M., Biescas E., Fernández I., Torrobella I., Crippa B., 2003b. Deformation control using SAR interferometry: quantitative aspects. Proceedings of Fringe 2003, ESA, 2-5 September 2003, Frascati (Italy).

Ferretti A., Prati C., Rocca F., 2000. Nonlinear subsidence rate estimation using permanent scatterers in differential SAR interferometry. *IEEE Transactions on Geoscience and Remote Sensing*, Vol. 38, No. 5, pp. 2202-2212.

Ferretti A., Prati C., Rocca F., 2001. Permanent scatterers in SAR interferometry. *IEEE Transactions on Geoscience and Remote Sensing*, Vol. 39, No. 1, pp. 8-20.

Goldstein R.M., Englehardt H., Kamb B., Frolich R.M., 1993. Satellite radar interferometry for monitoring ice sheet motion: application to an Antarctic ice stream. *Science*, Vol. 262, pp. 1525-1530.

Hanssen R., 2001. *Radar interferometry.* Kluwer Academic Publishers, Dordrecht (The Netherlands).

Massonnet D., Rossi M., Carmona C., Adragna F., Peltzer G., Felgl K., Rabaute T., 1993. The displacement field of the Landers earthquake mapped by radar interferometry. *Nature*, Vol. 364, pp.138-142.

Strozzi T., Wegmuller U., Tosi L., Bitelli G., Spreckels V., 2001. Land subsidence monitoring with differential SAR interferometry. *Photogrammetric engineering and remote sensing*, Vol. 67, No. 11, pp. 1261-1270.

Rosen P.A., Hensley S., Joughin I.R., Li F.K., Madsen S.N., Rodríguez E., Goldstein R.M., 2000. Synthetic Aperture Radar Interferometry. *Proceedings of the IEEE*, Vol. 88, No. 3, pp. 333-382.